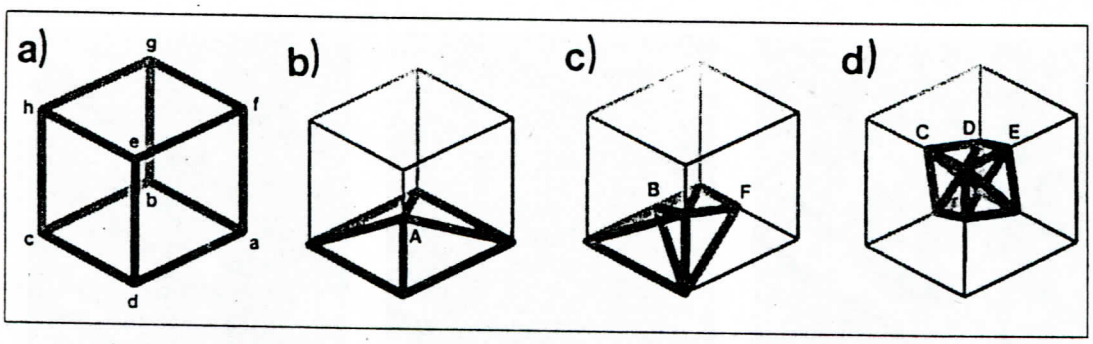

Figure 3. The OR *inner space domains (a)* $v_o^\perp$, *(b)* $v_{o1}^\perp$, *(c)* $v_{o2}^\perp$ *and* $v_{o1}^\perp$, *and (d)* $v_{o0}^\perp$.

$$F_T(\mathbf{Q}^\perp)=\sigma e^{i\mathbf{Q}^\perp\cdot\mathbf{r}_0^\perp}\prod_{j=1}^{3} e^{iQ_j^\perp}\frac{\sin Q_j^\perp}{Q_j^\perp}, \tag{13}$$

where $\sigma \equiv \text{sign}[\mathbf{a}_1^\perp\cdot(\mathbf{a}_2^\perp\times\mathbf{a}_3^\perp)]$ and $Q_j^\perp \equiv \frac{1}{2}\mathbf{Q}^\perp\cdot\mathbf{a}_j^\perp$.

Next we consider PR's and OR's that are inside an RD. A specific RD spanned by $a\hat{\mathbf{e}}_1$, $a\hat{\mathbf{e}}_2$, $a\hat{\mathbf{e}}_3$, and $a\hat{\mathbf{e}}_6$ is shown in Fig. 1. The inner space domain $v_{p1}^\perp$ corresponding to the singled out PR that is a part of the RD, is shown in Fig. 2(b). It can be decomposed into two tetrahedra, *Oedg* and *Odec*, with the coordinates of the vertices listed explicitly in Table II. There are six equivalent such domains associated with the PR contained in six differently oriented RDs. However, no two of these domains intersect, demonstrating that a PR is never shared simultaneously by two different RDs. On the other hand, if we subtract from $v_p^\perp$ the six equivalent domains of the type $v_{p1}^\perp$ we get the domain $v_{p0}^\perp$, in Fig. 2(c) that corresponds to these PRs that are not inside any RDs. This domain can be decomposed into the six tetrahedra *OPaf*, *OPbf*, *OPbe*, *OPce*, *OPcd*, and *OPad*. We use a decomposition of domains $v_T^\perp$ into tetrahedra to calculate their volumes and Fourier transforms (structure factors) given by Eq. (9). Thus, we obtain $v_{p1}^\perp = \frac{2}{3}a^3\eta^3$ and $v_{p0}^\perp = 2a^3\eta^3\tau^{-1}$, for the inner space volumes, and $n_{p1}=\frac{1}{30}\tau^{-3}$ and $n_{p0} = \frac{1}{10}\tau^{-4}$, for the number densities of corresponding PRs in the physical space. An explicit formula for the Fourier transform of any tetrahedron can be easily determined. Alternatively, the Fourier transform of any polyhedral domain can be equally easily calculated from a specification of its boundary, for example, by using the algorithm of Ref. 44.

Table IV. Coordinates of the vertices shown in Fig. 3 for the inner space domains $v_{\text{OR}}^\perp$. **For an explanation of the notation see Table II.**

Vertex	$(r_1^\perp,\ldots,r_6^\perp)$	$(x^\perp,y^\perp,z^\perp)$
A	$(-1,-1,0,0,0,0)$	$(-2,0,0)$
B	$(-1,0,1,0,-1,0)$	$(-1-\tau,1-\tau,\tau-1)$
C	$(0,0,1,1,0,0)$	$(-\tau,1-\tau,1)$
D	$(0,1,1,0,0,1)$	$(1-2\tau,0,\tau)$
E	$(0,0,0,0,1,1)$	$(-\tau,\tau-1,1)$
F	$(-1,0,0,-1,0,1)$	$(-1-\tau,\tau-1,\tau-1)$
a	$\frac{1}{2}(-1,-1,1,-1,1,1)$	$(-1-\tau,\tau,0)$
b	$\frac{1}{2}(-1,-1,1,1,1,1)$	$(-1-\tau,0,1)$
c	$\frac{1}{2}(-1,-1,1,1,-1,1)$	$(-1-\tau,-\tau,0)$
d	$\frac{1}{2}(-1,-1,1,-1,-1,1)$	$(-1-\tau,0,-1)$
e	$\frac{1}{2}(-1,1,1,-1,-1,1)$	$(-\tau,0,\tau-1)$
f	$\frac{1}{2}(-1,1,1,-1,1,1)$	$(-\tau,\tau,\tau)$
g	$\frac{1}{2}(-1,1,1,1,1,1)$	$(-\tau,0,\tau+1)$
h	$\frac{1}{2}(-1,1,1,1,-1,1)$	$(-\tau,-\tau,\tau)$

The inner space domain $v_{o1'}^\perp$, which corresponds to the singled out OR that is a part of the RD, is shown in Fig. 3(b). It can be decomposed into two tetrahedra, one with vertices *Abcd* and the other with *Adab*. Again, there are six equivalent such domains, each one associated with the OR contained in one of the six differently oriented RDs. Two of such domains may intersect, giving the region $v_{o2}^\perp$ that is the tetrahedron *ABcd* shown in Fig. 3(c). Therefore, this region is associated with the OR that is simultaneously a part of two different RDs. However, no three domains of the type $v_{o1'}^\perp$ intersect, demonstrating that an OR is never shared simultaneously by three different RDs. By subtracting $v_{o2}^\perp$ from $v_{o1'}^\perp$, one obtains the domain $v_{o1}^\perp$, associated with the ORs that are only inside a single RD. The domain $v_{o1}^\perp$ can be split into two tetrahedra, *ABbd* and *AFbd*, shown in Fig. 3(c). On the other hand, if we subtract from $v_o^\perp$ the six equivalent domains of the type $v_{o1'}^\perp$, we get the domain $v_{o0}^\perp$, which can be split into the six tetrahedra *ebAB*, *ebBC*, *ebCD*, *ebDE*, *ebEF*, and *ebFA*, shown in Fig. 3(d). The domain $v_{o0}^\perp$ corresponds to these ORs that are not inside any RDs. The vertices shown in Fig. 3 are listed in Table IV. The resulting inner space volumes are $v_{o1'}^\perp = \frac{2}{3}a^3\eta^3 = v_{p1}^\perp$, $v_{o2}^\perp=\frac{1}{3}a^3\eta^3\tau^{-1}$, $v_{o1}^\perp=\frac{2}{3}a^3\eta^3\tau^{-2}$, and $v_{o0}^\perp = 2a^3\eta^3\tau^{-3}$, which after division by $v_{\text{RT}}^\perp$ yield the number

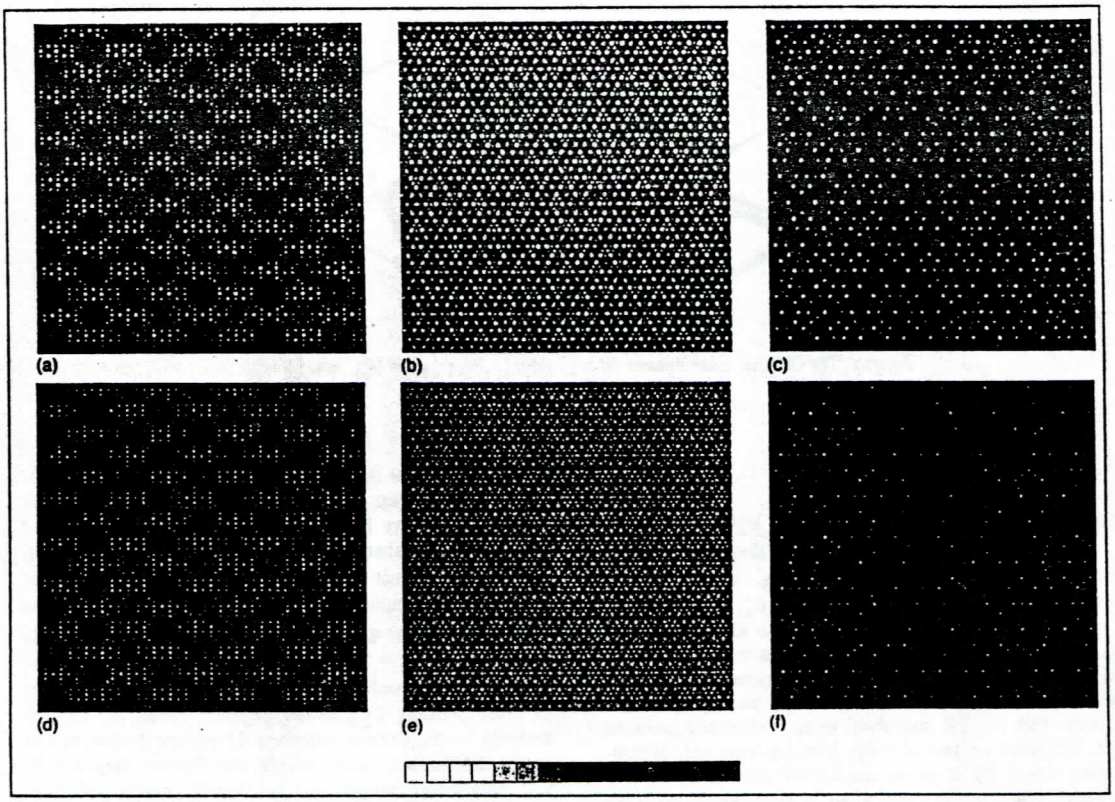

Figure 4. Reconstructed electron (first row) and nuclear (second row) densities, Ref. 13 are shown in the physical space projected from a 90 Å×90 Å wide, 50 Å thick slab perpendicular to a twofold (first column), a threefold (second column), or a fivefold (third column) symmetry axis. The black in the gray scale at the bottom of the figure corresponds to the lowest values of the density (-0.844 eÅ^{-3} for the first row, and -1.111×10^{-5} Å^{-2} for the second row), while the white corresponds to the highest values (6.645 eÅ^{-3} for the first row, and 3.249×10^{-5} Å^{-2} for the second row).

densities of the associated ORs as $n_{o1'} = \frac{1}{30}\tau^{-3} = n_{p1}$, $n_{o2} = \frac{1}{60}\tau^{-4}$, $n_{o1} = \frac{1}{30}\tau^{-5}$, and $n_{o0} = \frac{1}{10}\tau^{-6}$.

II. RESULTS AND DISCUSSION

A. Data and phase reconstruction

The formalism presented in the previous section will be applied here to i($Al_{0.570}Cu_{0.108}Li_{0.322}$). The neutron scattering length per unit volume ("nuclear density") and the number of electrons per unit volume ("electron density") will be determined from the neutron and x-ray diffraction data,[12] respectively, and analyzed both in the physical space and in the hyperspace. The i($Al_{0.570}Cu_{0.108}Li_{0.322}$) structure factors were reconstructed in Refs. 13 and 14 using the published x-ray and neutron diffraction data sets consisting of 56 and 40 icosahedrally independent intensities, respectively.[12,45] The hypercrystal associated with i($Al_{0.570}Cu_{0.108}Li_{0.322}$) is a six-dimensional simple hypercubic crystal with the lattice constant $\tilde{a}=7.15$ Å. Therefore, the corresponding Ammann rhombohedra have the edges of length $a=5.06$ Å. The required matching in the hyperspace between the Wyckoff sites of the tiling and those of the reconstructed density limits the choice of the location of the tiling relative to the density to two possibilities. They are related by a translation half-way along a body diagonal of the hypercubic unit cell. Based on the Y_h site symmetry, we shall identify the center of the RT with the vertex location of the reconstructed density. Its identification with the body center location does not result in a density distribution consistent with the tiling assumption.

It is well known that the limited range of the experimentally accessible reciprocal space, the inevitable diffraction intensity truncations at the limit of instrumental sensitivity, or the limited sampling of the reciprocal space in the experiment, will all affect the accuracy of the reconstructed scatterer densities, especially in quasiperiodic crystals.[46–49] For example, as discussed in Ref. 46, the truncation is mainly responsible for occasional negativity of the reconstructed electron densities. A particularly important effect of the truncation is the limited resolution with which hyperatom shapes in the inner space, and tile decorations in the physical space, can be extracted from the reconstructed

densities. The experimental data that we use here are limited in the reciprocal space to $Q<10$ Å^{-1} and $Q^{\perp}<0.8$ Å^{-1}.[46] This means that some features that may be observed in the reconstructed density on the scales up to $2\pi/Q\sim0.6$ Å, in the physical space, and up to $2\pi/Q^{\perp}\sim7.8$ Å, in the inner space, could be caused by the limited range of the experimental data. The truncation effects could be modestly alleviated by an extrapolation of the experimental data to somewhat larger values of the scattering vector $\bar{Q}$ by the method suggested in Ref. 14. However, it is clear that experimental improvements and much more extensive diffraction data are needed in order to reconstruct more reliable quasicrystal densities.

The removal of thermal fluctuations from the reconstructed densities, by factoring out of the structure factor an overall thermal Debye–Waller factor as described earlier in Eq. (6), is expected to increase the sharpness of the features in the reconstructed densities. However, since this factoring out would generally increase values of the structure factor at the truncation boundary, the relative importance of the truncation effects would increase accordingly. Indeed, after deconvoluting according to Eq. (6) the physical and inner space Debye–Waller factors determined in Ref. 13, we verified an increase in the amplitude of fluctuations in the reconstructed densities on the scales of ≈0.6 and ≈7.8 Å in the physical and inner spaces, respectively. Consequently, we shall focus below only on the results obtained without any deconvolution of thermal fluctuations.

Before proceeding with a detailed analysis of the reconstructed densities, it would be useful to first lend support to the phase reconstruction[13,14] we used to generate our data. This could be best accomplished by considering experimental data that are, unlike the diffraction intensities, dependent on the phases. For this purpose, we can use HRTEM images which are available for $i(Al_{0.570}Cu_{0.108}Li_{0.322})$.[50,51] Projections of the reconstructed electron densities from a 50 Å thick slab of quasicrystal perpendicular to the twofold, threefold, and fivefold symmetry axes onto a plane parallel to the slab are shown in Figs. 4(a)–4(c) using the phase reconstruction of Ref. 13. They are in a good qualitative agreement with the transmission electron micrographs obtained in Refs. 50 and 51, lending a more direct support for the validity of the phase reconstruction. However, a more realistic simulation of the HRTEM images based on the potentials inferred from the reconstructed density is necessary before more definitive conclusions can be drawn about the validity of the reconstructed phases. For example, the appropriate HRTEM calculations, like the ones that have been performed for some quasicrystal models,[51,52] would have to include the effects such as defocusing and multiple scattering. Nevertheless, two-dimensional projections of the reconstructed densities are useful in their own right as they can help discern certain structural motifs, such as stacks of atoms or, conversely, channels in the structure. Therefore, in addition to the projections of the electron densities, we also show in Figs. 4(d)–4(f) projections of the nuclear densities obtained using the phase reconstruction of Ref. 13. Similar figures are obtained using the reconstruction of Ref. 14.

B. 2D hypercrystal planes

We shall begin our analysis of the reconstructed $i(Al_{0.570}Cu_{0.108}Li_{0.322})$ quasiperiodic densities in the hyperspace. It is useful to examine the densities inside the two-dimensional twofold, threefold, and fivefold rotation planes placed at V or B. The densities are periodic in these planes, with one axis in the physical space and the perpendicular axis in the inner space, as shown in Fig. 5. These rotation planes are also crystal planes of the hypercrystal. The twofold symmetry plane is spanned by the hyperlattice vectors $\tilde{a}(110000)$ and $\tilde{a}(001001)$, so that its horizontal axis is the x axis of the physical space, while the vertical axis is the $x^{\perp}$ axis of the inner space. The threefold symmetry plane is spanned by the hyperlattice vectors $\tilde{a}(101100)$ and $\tilde{a}(010011)$, and its horizontal axis is along the physical space [111] direction, while its vertical axis is along the inner space $[111]^{\perp}$ direction. The fivefold symmetry plane is spanned by the hyperlattice vectors $\tilde{a}(100000)$ and $\tilde{a}(011111)$, so that its horizontal axis is along the physical space $[\tau 01]$ direction, while its vertical axis is along the inner space $[10\bar{\tau}]^{\perp}$ direction. These planes contain the high symmetry points of the hypercubic lattice, which are the centers of n cubes, $n=0,1,2,\ldots,6$. In addition to a V at (000000) ($n=0$) seen in all figures except those in the first column, an E at $\frac{1}{2}(100000)$ ($n=1$) seen in all figures in the fourth column, and a B at $\frac{6}{2}(111111)$ ($n=6$) seen in all figures in the first, third, and fourth columns, these planes contain: $\frac{2}{2}(110000)$ ($n=2$) seen in all figures in the first and second columns; $\frac{3}{2}(101100)$ ($n=3$) seen in all figures in the third column; $\frac{4}{2}(111001)$ ($n=4$) seen in all figures in the first and second columns, and $\frac{5}{2}(011111)$ ($n=5$) seen in all figures in the fourth column. Therefore, these planes offer a systematic and extensive view through the hypercrystal density.

The electron and nuclear densities reconstructed using the method of Ref. 13, and the nuclear density reconstructed using the method of Ref. 14, are shown in Fig. 5. As can be seen from this figure, the reconstructed $i(Al_{0.570}Cu_{0.108}Li_{0.322})$ hypercrystal density is remarkably simple. It is mainly concentrated in narrow bands whose width is on the order of ≈1 Å around three-dimensional planes parallel to the inner space. For the electron densities, these three planes are centered on the vertices and the edge centers of the hypercubic lattice. The same three planes of high positive density are also seen in the nuclear densities, but there are additional planes of large negative nuclear densities centered at the body centers of the hypercubic lattice. We interpret these densities as arising from hyperatoms located at V, E, and B. Since Li is a very weak x-ray scatterer compared to Al and Cu and, unlike Al and Cu, it has a negative scattering length for neutrons, the large positive densities found at V and E for both electron and nuclear densities, suggest that the associated hyperatoms are mainly composed of Cu and Al. A large negative nuclear density at B, combined with the absence of a high electron density there, is consistent with the assumption that the B hyperatom is dominated by Li.

We found little noticeable difference between the nuclear densities reconstructed using the two different methods, Refs. 13 and 14. Therefore, we shall analyze below only the densities reconstructed by the method of Ref.

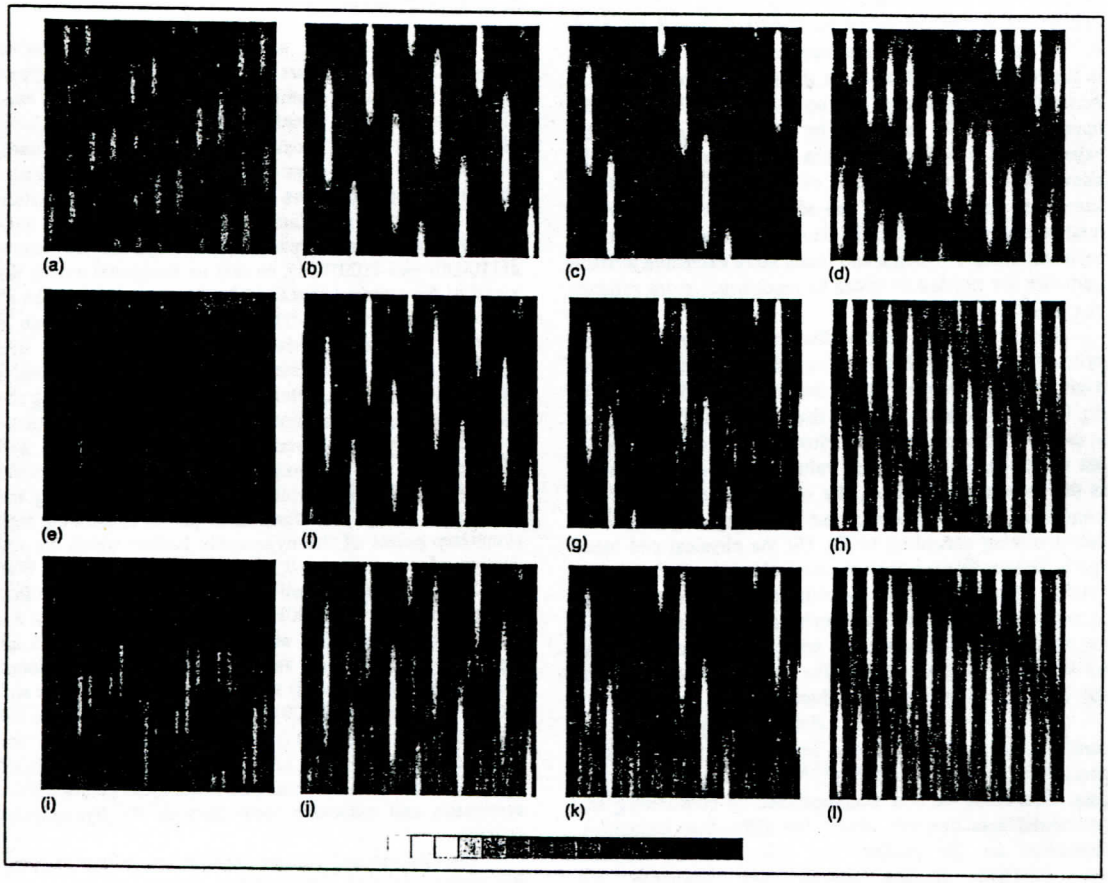

Figure 5. Reconstructed electron (Ref. 13) (first row) and nuclear (Refs. 13 and 14) (second and third rows) densities. Two-dimensional twofold (first two columns), threefold (third column), and fivefold (fourth column) rotation planes are shown. The upper left-hand corners of the plates shown in the first column are at B, while in the remaining three columns they are at V. The black in the gray scale at the bottom of the figure corresponds to the lowest values of the density ($-6.434\ e\text{Å}^{-3}$ for the first row, $-10.010\times10^{-5}\ \text{Å}^{-2}$ for the second row, and $-11.713\times10^{-5}\ \text{Å}^{-2}$ for the third row), while the white corresponds to the highest values ($42.441\ e\text{Å}^{-3}$ for the first row, $33.805\times10^{-5}\ \text{Å}^{-2}$ for the second row, and $34.530\times10^{-5}\ \text{Å}^{-2}$ for the third row).

13, where the structure factors for both electron and nuclear densities were determined.

C. Inner-space density

After noticing in Fig. 5 that the high scatterer densities extend over the three-dimensional inner spaces located at V, E, or B, it becomes necessary to examine the densities inside these spaces. The reconstructed inner space densities at V, E, and B, can help further elucidate shapes and chemical compositions of the hyperatoms. Isodensity surfaces and two-dimensional slices through the inner space densities at V, E, and B are shown in Fig. 6.

The nuclear density at V is essentially spherical, due to a relatively small number of structure factors measured with neutron diffraction. However, the electron density at V reveals the Y_h site symmetry and is slightly extended along the fivefold axes, indicating that the associated hyperatom is also extended along these axes. Consequently, the isosurface shown in Fig. 6(c) has the shape of a slightly rounded icosahedron. The electron density also shows a clear depression at the center of the icosahedron, indicating that the associated hyperatom might have a hollow center.

Similarly, while the nuclear density at E has a form of a slightly oblate ellipsoid of revolution around the fivefold symmetry axis, the electron density reveals the D_{5d} site symmetry more clearly. The electron density is slightly extended along the five twofold axes in the (equatorial) plane perpendicular to the fivefold axis. This can be also seen in the isodensity surface shown in Fig. 6(g). The shape of this surface resembles the intersection of two rounded icosahedra, each similar to the one shown in Fig. 6(c), that are displaced along the fivefold axis.

While there is essentially no electron density at B, the nuclear density is strongly negative there. It extends along the threefold axes resulting in the isosurface shown in Fig.

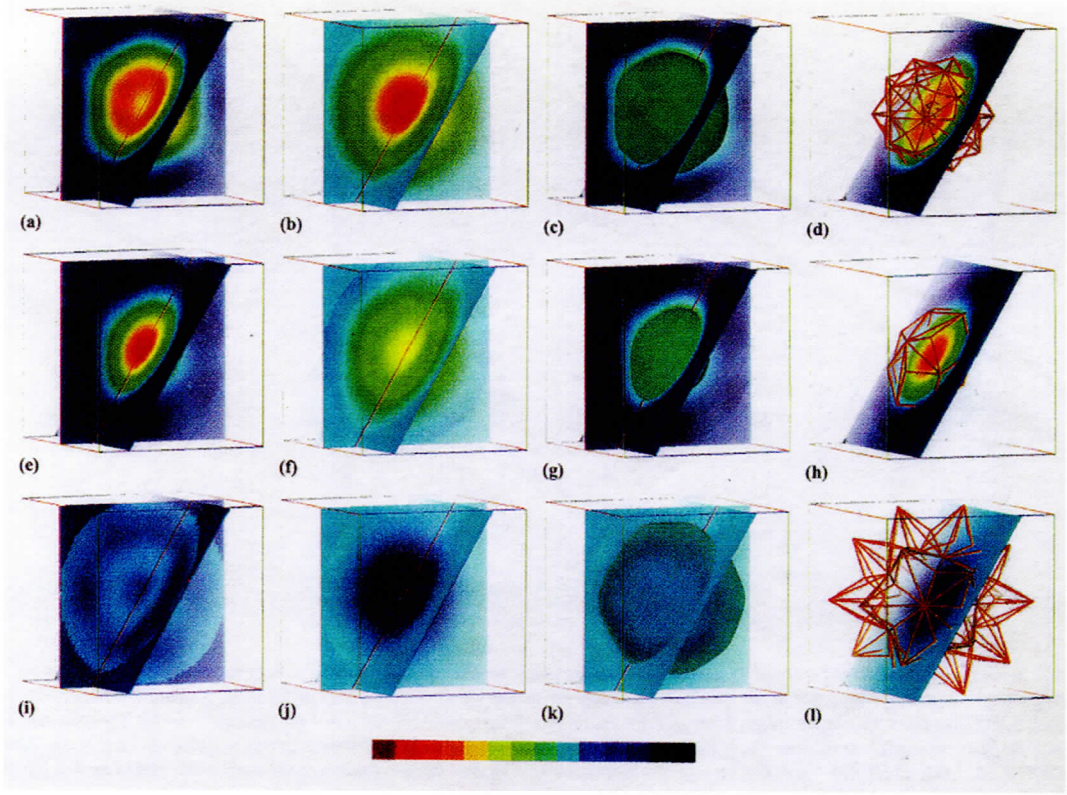

Figure 6. Reconstructed electron (first column) and nuclear (second column) densities in the inner space centered at V (first row), E (second row), and B (third row). Densities in two two-dimensional slices, one perpendicular to a twofold symmetry axis and the other perpendicular to a fivefold symmetry axis, are shown. The densities were calculated inside a sphere of diameter 22.52 Å and outside of it they were set to the average values, 0.697 $e\text{Å}^{-3}$ for the electron density, and 0.130×10^{-5} Å^{-2} for the nuclear density. The dark blue color shown in the color map at the bottom of the figure, corresponds to the minimum values of the density (-6.347 $e\text{Å}^{-3}$ and -10.010×10^{-5} Å^{-2}, for the electron and the nuclear density, respectively), while the red color corresponds to the maximum values of the density (42.441 $e\text{Å}^{-3}$ and 33.805×10^{-5} Å^{-2}, for the electron and the nuclear density, respectively). Isosurfaces of constant density are shown in the third column for the electron density equal to 10.000 $e\text{Å}^{-3}$ [(c) and (g)] and for the nuclear density equal to -0.400×10^{-5} Å^{-2} (k). For the sake of a comparison we also show edges of hyperatoms modeled in Ref. 15.

6(k) that is similar to a pentagonal dodecahedron with a slightly concave facets. There are no indications in either *B* or *E* densities of any depletion at the centers of their distributions.

These observations about the inner space densities are qualitatively consistent with the hyperatom shapes obtained in the model of Ref. 15, also shown in Fig. 6. However, they seem slightly more consistent with an alternative model also given in Ref. 15 in Appendix D. This is perhaps not suprising since the alternative model of Ref. 15 gives all phases consistent with these obtained by the reconstruction,[13] while the other model has the opposite phases for two, albeit weak, x-ray structure factors.

In order to obtain a somewhat more discriminating information about the stoichiometry of the hyperatoms, using Eqs. (4) and (5), we projected onto the inner space the densities from the physical space within a sphere of radius $r=0.5$ Å centered at the inner space.[17] This radius was chosen so as to be sufficiently large to include some smearing of the hyperatoms due to their shape or (thermal) disordering in the physical space but not too large so that densities from the nearby hyperatoms are included. We are interested in the resulting values obtained in the inner spaces centered, again, at *V*, *E*, and *B*. Within the expected accuracy of the reconstructed densities, which is affected by the truncation and disordering in the inner space, the peak values of these projected densities found at *V*, *E*, and *B* support the conclusion that *B* consists mainly of Li, while *V* and *E* consist mainly of Cu and Al, with a larger concentration of Cu at *V*.

D. Physical space density

Several of the models of i($Al_{0.570}Cu_{0.108}Li_{0.322}$) structure discussed in Ref. 15 have qualitatively similar hyperatoms that are consistent with our inner space density analysis. Our next step is to analyze the reconstructed densities in the physical space. Therefore, we calculated densities in the

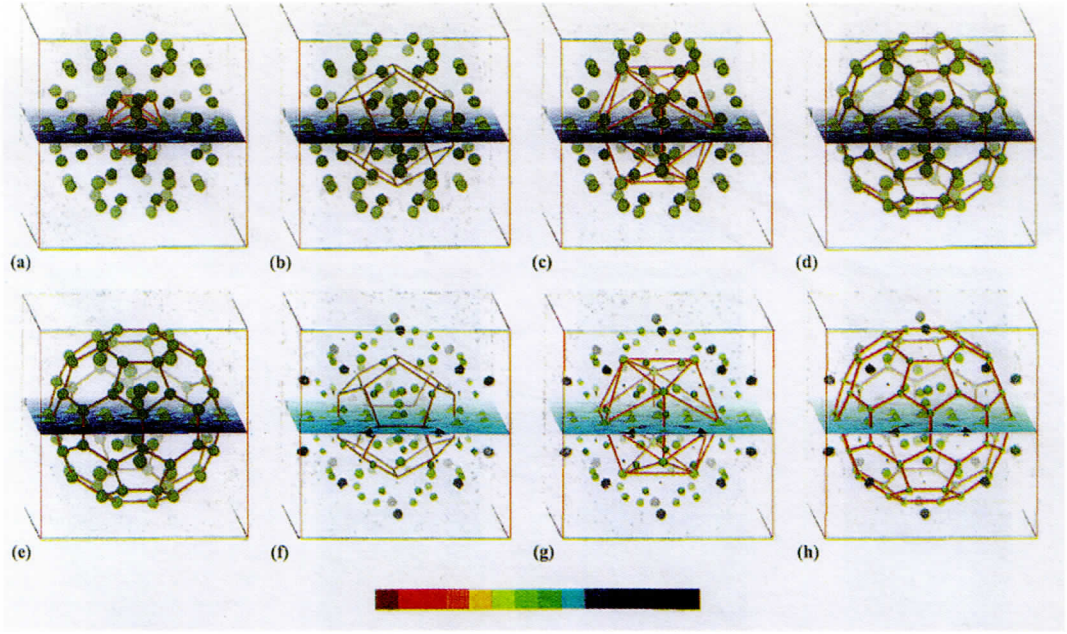

Figure 7. Reconstructed electron (first row) and nuclear (second row) densities in the physical space centered at V. Denisities inside a two-dimensional slice perpendicular to a twofold symmetry axis of the icosahedral symmetry are shown. The densities were calculated inside a sphere of diameter 15.6 Å and outside of it they were set to the average values, 0.697 $e\text{Å}^{-3}$ for the electron density, and 0.130×10^{-5} Å^{-2} for the nuclear density. The color map at the bottom of the figure corresponds to the same density ranges as in Fig. 6. We also show isosurfaces of electron density of 10.000 $e\text{Å}^{-3}$ and nuclear densities of 7.000×10^{-5} Å^{-2} and -3.500×10^{-5} Å^{-2}. For the sake of a comparison we also show the lines connecting the atoms within each of the first four shells of atoms found around a V site in Ref. 15.

physical space centered at *V*, *E*, and *B*, and shown in Figs. 7–9. We chose these points since they are among the highest symmetry points in i($Al_{0.570}Cu_{0.108}Li_{0.322}$). Moreover, the clusters centered at these points were investigated in the model of Ref. 15. Some of the highest density regions seen in the physical space that are surrounded by nearly spherical isosurfaces indicate likely locations of the atoms in the quasiperiodic i($Al_{0.570}Cu_{0.108}Li_{0.322}$). Moreover, Li is likely to be associated with the regions of high negative nuclear density, while Al and Cu are likely to be associated with the regions of high positive nuclear and electron densities. Regions of somewhat lower, but still peaked, densities are more likely to be manifestations of the "phason" disorder in the structure.

The physical space densities centered at *V* and displayed in Fig. 7 are similar to the densities reconstructed for the known crystal structure of R($Al_{0.564}Cu_{0.116}Li_{0.320}$).[53] This serves as a self-consistency check for the used structure factor reconstruction method,[13] which assumes that atomic clusters found in the crystal are similar to those that exist in the quasicrystal. As a guide to the eye, also shown in Fig. 7 are the lines connecting the atoms found within the first four shells surrounding a *V* site in the model of Ref. 15. Such clusters are found in several models reviewed in Ref. 15, and it is interesting to note that the second (dodecahedral) shell of Li atoms appears slightly contracted relative to a shell of (weak) negative density peaks that can be seen in the figure. This is consistent with what is noted in Figs. 5(g) and 5(k), where we can identify a splitting of the negative density at *B* along a threefold axis in the physical space. However, it is not possible to conclude with certainty whether this observation implies a possible nonflatness of the *B* hyperatom, a possible partially occupied "double well" hyperatom, or whether it is simply an artifact of the limited range of Fourier components that are available for the reconstruction.

The quasiperiodic i($Al_{0.570}Cu_{0.108}Li_{0.322}$) must also contain local environments which are not present in R($Al_{0.564}Cu_{0.116}Li_{0.320}$). Such is the D_{5d} fivefold symmetric environment centered at *E* and shown in Fig. 8. It is consistent with the structure model of Ref. 15. An icosahedral cluster centered at *B* was also investigated in Ref. 15. Although atomic sites in its first three shells shown in Fig. 9 were occupied only when the cluster was shifted slightly off the exact *B* site, a finite occupancy of these sites is expected due to the phason disordering. Indeed, we see that the reconstructed densities are peaked at, or near, all of these atomic sites. On the contrary, all the sites in the fourth shell are occupied in the model by Li even when the shell is centered exactly at *B*. (This is also true for the fifth and sixth shells which can be easily identified in the figure, but are not connected.) However, we cannot detect any nega-

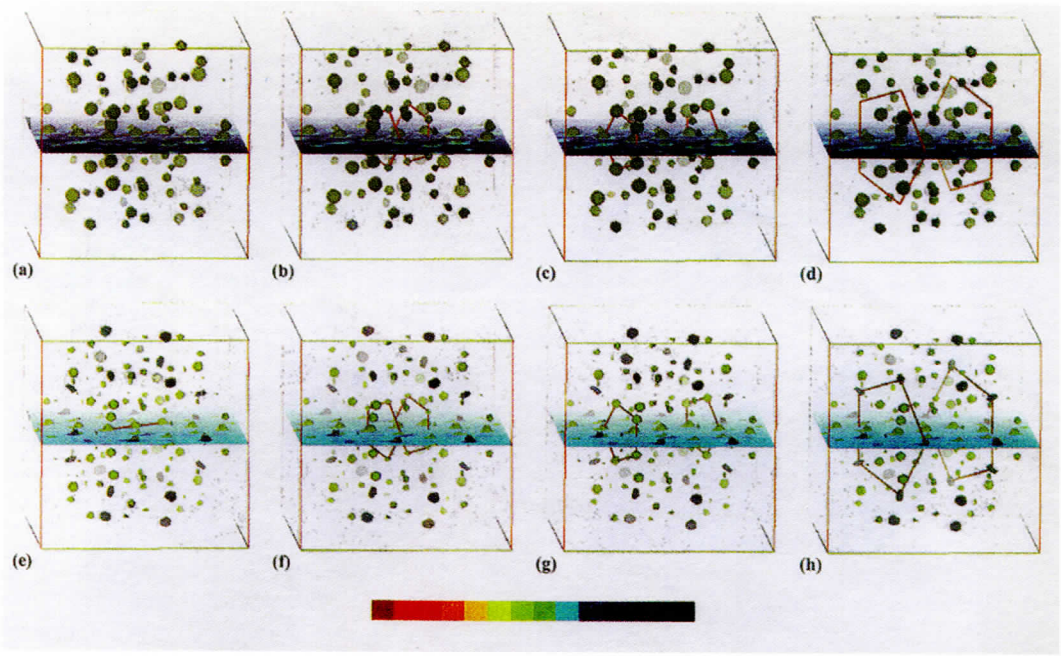

Figure 8. Reconstructed electron (first row) and nuclear (second row) densities in the physical space centered at E. See the caption of Fig. 7.

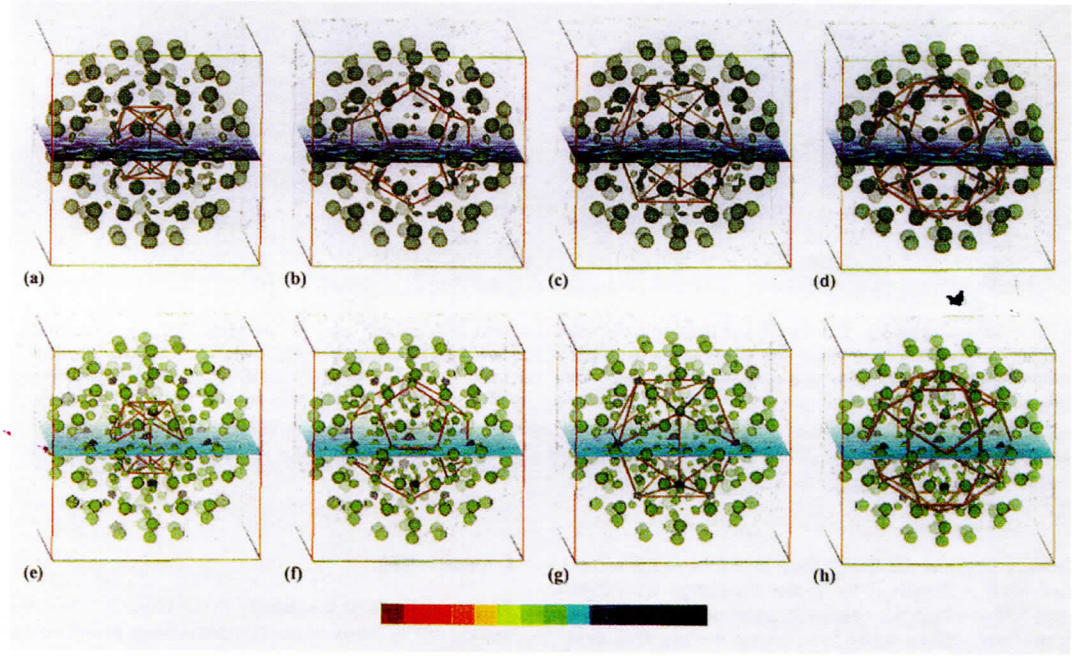

Figure 9. Reconstructed electron (first row) and nuclear (second row) densities in the physical space centered at B. See the caption of Fig. 7, except that we show here isosurfaces of electron density of 6.000 $e\text{Å}^{-3}$ and nuclear densities of 3.000×10^{-5} Å^{-2} and -3.500×10^{-5} Å^{-2}.

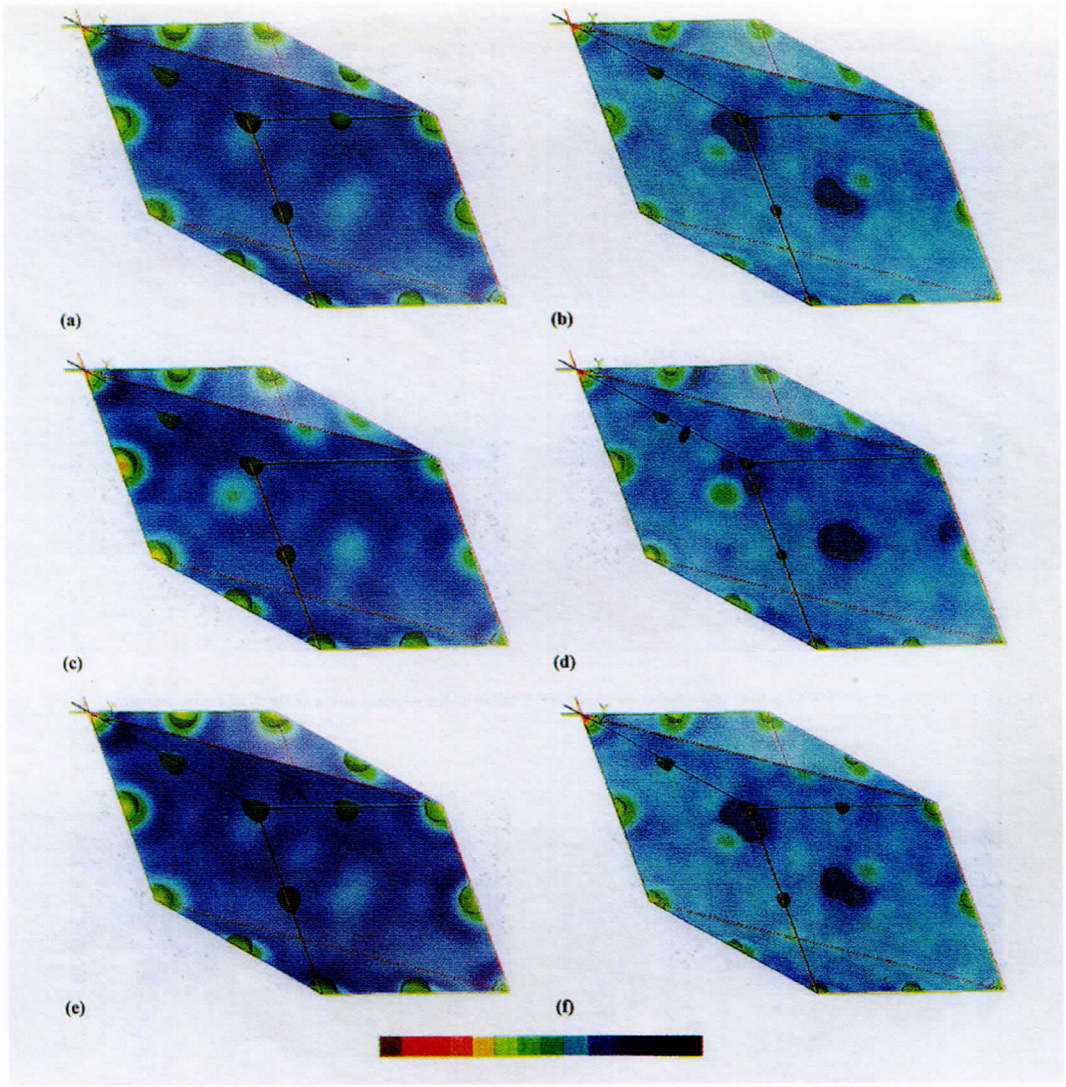

Figure 10. Reconstructed electron (first column) and nuclear (second column) densities in the physical space on the average PR *in a particular orientation. Results of averaging over* PRs *in any local environment (first row), inside an* RD *(second row), and outside any* RD *(third row), are shown. Densities within the* PR *mirror plane oHCp and within its three rhombic faces, pAJC, oHJA, and JHEC, are shown. The labels and the relative orientations of* PR *and* RD *are the same as in Fig. 1. We also show isosurfaces of electron density of 14.318 eÅ^{-3} and nuclear densities of 10.850×10^{-5} Å^{-2} and −2.430×10^{-5} Å^{-2}. The dark blue color shown in the color map at the bottom of the figure, corresponds to the minimum values of the density (−4.365 eÅ^{-3} and −7.017×10^{-5} Å^{-2}, for the electron and the nuclear density, respectively), while the red color corresponds to the maximum values of the density (40.911 eÅ^{-3} and 31.451×10^{-5} Å^{-2}, for the electron and the nuclear density, respectively).*

tive density peaks at the fourth shell locations in the reconstructed nuclear density. This is also consistent with Figs. 5(e) and 5(i) in which the Li sites in question can be located along the twofold symmetry axes where the negative density practically blends into the background. Therefore, it might be necessary to examine the model *B* hyperatom more closely along its twofold symmetry axes.

E. Ammann tiling

Further analysis of the density in the physical space will be carried out in terms of the Ammann tiling described earlier in Sec. I B. Using the results of that section we calculated the electron and nuclear densities inside rhombohedra of a particular orientation that either are, or are not, contained

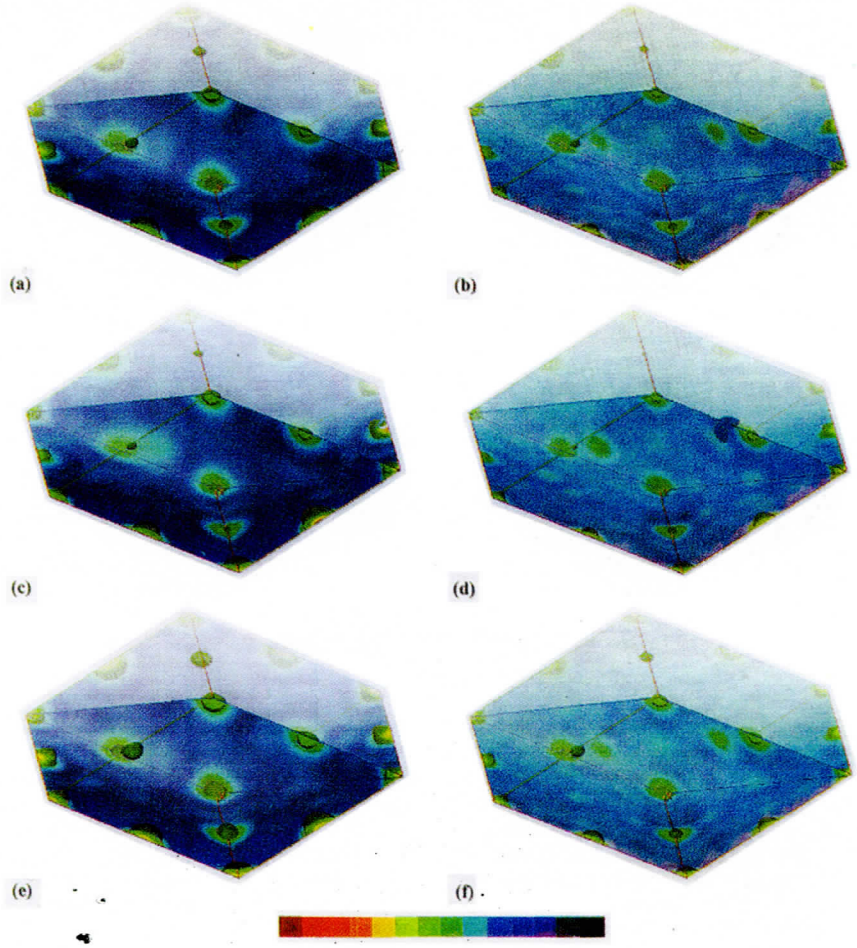

Figure 11. Reconstructed electron (first column) and nuclear (second column) densities in the physical space on the average OR *in a particular orientation. Results of averaging over* ORs *in any local environment (first row), inside an* RD *(second row), outside any* RD *(third row), simultaneously inside two* RD *(forth row), and inside a single* RD *(fifth row) are shown. Densities within the* OR *mirror plane IFoB and within its three rhombic faces, oBGK, oKFH, and oHEB, are shown. We use the same notation, colormap, and the isosurface values as in Fig. 10.*

inside some RD. Our results are shown in Figs. 10 and 11 for PR and OR, respectively. We also calculated density variances for these rhombohedra and we show nuclear density variances for PR and OR in Figs. 12 and 13, respectively.

First, we consider general PR and OR whose densities are shown in Figs. 10(a) and 10(b) and 11(a) and 11(b), respectively. The densities inside average PR and OR that are shown in these figures have the correct D_{3d} symmetries. The positive densities are peaked at vertices and edge centers, indicating that these positions might be occupied by Al or Cu. The negative nuclear densities are peaked mainly along the threefold diagonal of the PR, dividing it into three segments approximately in the ratio $\tau:1:\tau$, and indicating that these positions are likely occupied by Li. The vertex and midedge positions of Al and Cu, and the PR diagonal position of Li were suggested in several atomic structure models of $i(Al_{0.570}Cu_{0.108}Li_{0.322})$.[54] However, several features of the densities suggest that a more complicated decoration of the tiles might be necessary to accurately model $i(Al_{0.570}Cu_{0.108}Li_{0.322})$. For example, the peaks of the negative nuclear density along the PR's threefold body diagonal are split around the positions that correspond to the "ideal" ratio $\tau:1:\tau$. This is fully consistent with the splitting along the threefold axes in the physical space that we already noted in Figs. 5(g) and 5(k) and discussed in Sec. II B. We also observe in Figs. 12(a) and 13(a) a relatively large nuclear density variances in these tiles, not only at vertices,

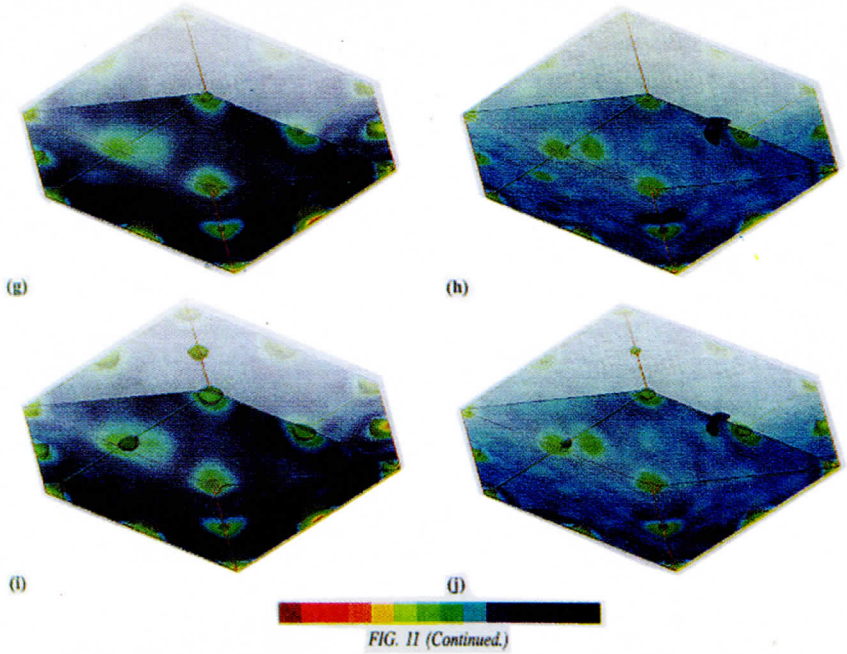

FIG. 11 (Continued.)

edge centers and near the PR body diagonal sites, but also at the PR facets and, to a lesser extent, in the mirror planes of the OR. These large density variances and the apparent splitting of the "ideal" Li locations could result from "phason" disordering of the quasicrystal structure. However, a possibility that these large variances reflect the existence of different atomic decorations of tiles located in different local environments must be also investigated.

Indeed, as we look at PRs and ORs in more specific environments, namely, those that are either inside or outside an RD, the density peaks become more pronounced and the density variances are reduced. For example, we show in Figs. 10(e) and 10(f) and 11(e) and 11(f) densities averaged over those PRs and ORs that are *not* inside any RD. The corresponding variances are shown in Figs. 12(c) and 13(c). These densities and variances again have the full D_{3d} symmetry of the rhombohedra. However, the major peaks in Figs. 10(e) and 10(f) and 11(e) and 11(f) are larger than in Figs. 10(a) and 10(b) and 11(a) and 11(b). At the same time the largest variances are reduced in Figs. 12(c) and 13(c) compared to Figs. 12(a) and 13(a). Therefore, we can conclude with more confidence that the ORs and PRs that are not inside any of the RD are likely to have Al or Cu at their vertices and edge centers, and Li along the threefold body diagonal of the PR.

The densities averaged over those PRs and ORs that *are* inside an RD are shown in Figs. 10(c) and 10(d) and 11(c) and 11(d), respectively. The corresponding variances are shown in Figs. 12(b) and 13(b). These densities and variances are significantly different from the ones for the PRs and ORs that are not inside an RD. The C_s symmetries of these PR and OR densities are clearly seen in the figures. The mirror symmetry planes are precisely the two mirror planes of the RD to which the PR and OR belong. The first RD mirror plane coincides with the mirror plane $oHCp$ of the PR and with the plane of the facet of $oKFH$ of the OR shown in Fig. 1. The second RD mirror plane coincides with the mirror plane $IFoB$ of the OR and with the plane of the facet $pBoA$ of the PR. It can be also easily verified that the density distributions are identical over the $oBEH$ faces of PR and OR. In comparison to the densities in Figs. 10(e) and 10(f) and 11(e) and 11(f), the main difference is that here the positive peaks are considerably reduced at the rhombohedron vertex o and at the centers of the edges oA, oB, oH, and oK that are in the interior of the RD. There are also changes in the negative nuclear density peaks. The PR threefold diagonal position of the peak close to the center of the RD has a much smaller splitting, while the other diagonal position splits around the ideal location more clearly. In addition, a new negative density peak of a significant size emerges slightly off the center of the edges Ho, close to the position that divides the edge in the "ideal" ratio τ:1, but slightly shifted along the mirror plane away from the edge. It is accompanied by a new negative density peak on the face $oKFH$ of OR slightly off a point that divides the edge Ho in the ratio τ:1.

These observations are partially consistent with the decoration of the RD suggested in Ref. 55 and implemented in the structure model of Ref. 16. In this model, the central vertex and the four edge center positions inside the RD are empty, while Li is placed at the edges Ho and Ko, dividing them in the ratio τ:1. However, we do not find any significant positive density peaks near the two sites close to the center of the RD, along its short twofold axis, where the

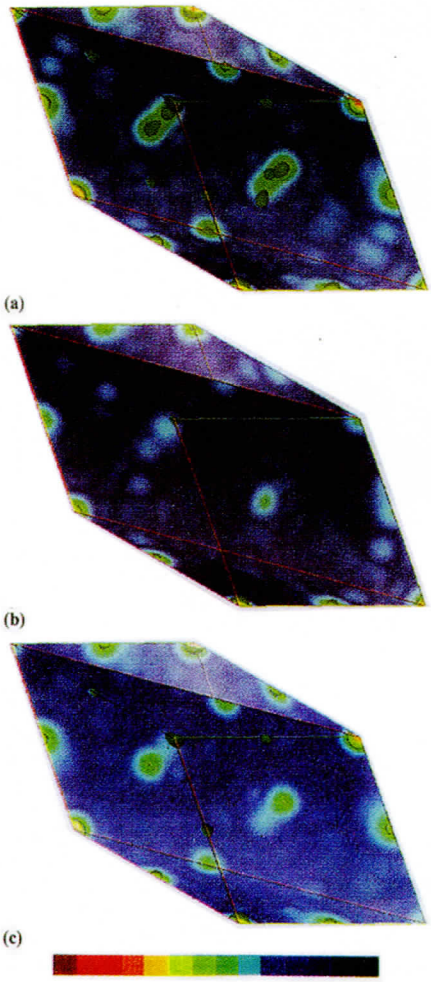

Figure 12. Variance of the reconstructed nuclear densities in the physical space on the average PRs *correspondings to Fig. 10. The dark blue color shown in the color map at the bottom of the figure corresponds to the minimum value of* 0.001×10^{-5} *Å*$^{-2}$, *and the red color corresponds to the maximum value of* 5.405×10^{-5} *Å*$^{-2}$ *of the density variance. We also show isosurfaces of the variance of* 2.700×10^{-5} *Å*$^{-2}$.

model of Ref. 16 predicts Al atoms. In the next subsection we shall discuss these Al sites in some more detail. Other discrepancies with the model can be also seen in the considerable negative density peaks that appear along the PR edges pA and pB and the OR edge FI dividing these edges in the ratio τ:1. However, the positions of some closely spaced density peaks cannot be occupied by atoms at the same time since they are too close. The high densities observed at such positions may be a result of the tile averaging, indicating that in some tiles one or the other of the two locations is occupied. Another possibility is that the tiling is disordered by tile rearrangements ("phasons") in the real material,[30,31] so that the density itself reflects sites which are not simultaneously occupied.

While the tile rearrangements are likely to be present in the real material, as suggested by the smearing of the densities in the inner space, a possible existence of different decorations of the RD must be further investigated. In contrast to a PR which is either outside an RD, or inside of precisely one RD, an OR can be also shared by two RDs. We show in Figs. 11(g) and 11(h) densities averaged over all ORs that are simultaneously inside two RDs and in Figs. 11(i) and 11(j) average densities inside those ORs that inside precisely one RD. The associated nuclear density variances are shown in Figs. 13(d) and 13(e). The densities in Figs. 11(i) and 11(j) have the same mirror symmetry and are generally similar to the densities in Figs. 11(c) and 11(d). The major difference is that the peaks at the vertices and the edge centers of the face $BEIG$ are enhanced. At the same time, the negative density peaks are slightly diminished while the nearby positive peaks are enhanced. The densities presented in Figs. 11(g) and 11(h) have a C_2 symmetry with the twofold rotation axis that connects the centers of the BG and HF edges. These densities show exactly the opposite tendencies to the densities in Figs. 11(i) and 11(j) that we just described. These observations are consistent with the corresponding decrease in the variances in Figs. 13(d) and 13(e) compared to Fig. 13(b) and with the interpretation that decorations of different types of PRs and ORs are different.

While we cannot fully determine the tile decorations from the present analysis, it appears that the tiling models of i($Al_{0.570}Cu_{0.108}Li_{0.322}$) structure are not yet complete.[15] In order to determine tile decorations more precisely, it would be necessary to examine RD and other tiling arrangements more closely. For example, densities within different RDs should be examined relative to the symmetries of their immediate surroundings, starting with the full symmetry group of RD (D_{2d}), down through all of its subgroups. Also, the presence or absence of 12-coordinated vertices should be probably considered an important attribute of tile arrangements. Such sites are found to be empty in the related crystalline structure of R($Al_{0.564}Cu_{0.116}Li_{0.320}$). In addition, it may be useful to examine as separate tiling units the arrangements of five PRs and five ORs into a rhombic icosahedron, or of ten PRs and ten ORs into a rhombic triacontahedron. However, much more extensive diffraction data sets are needed before meaningful conclusions can be extracted from such a detailed analysis.[14,15,46,49,56–58]

F. Where is Al?

One of the most promising tiling models of i($Al_{0.570}Cu_{0.108}Li_{0.322}$) structure[16] predicts 30 pure Al hyperatoms surrounding the body center Li hyperatom along its twofold symmetry axes. These Al hyperatoms give rise to two Al atoms inside RD, along its shorter twofold axis. As we already mentioned, we neither see signs of such Al in the inner space nor in the tiling density analysis. It was pointed out in Ref. 15 that the separation of the two Al atoms inside the RD as modeled in Ref. 16 is unphysically short. In fact, the two Al atoms are slightly more separated in the related crystalline R($Al_{0.564}Cu_{0.116}Li_{0.320}$) structure,

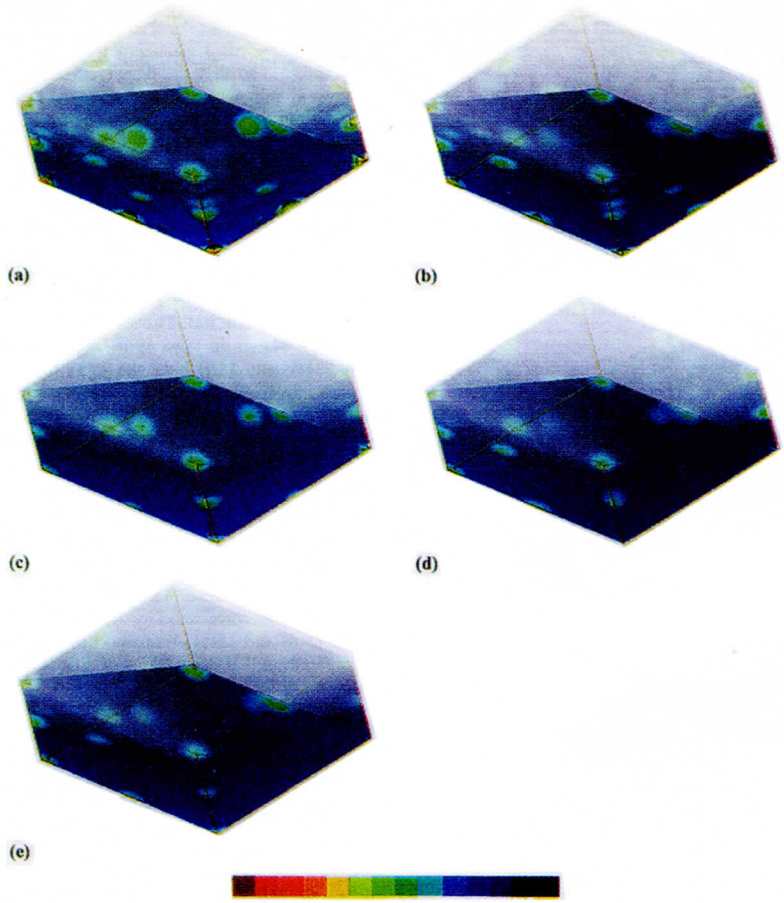

Figure 13. Variance of the reconstructed nuclear densities in the physical space on the average ORs *corresponding to Fig. 11. We use the same colormap as in Fig. 12.*

so that their positions, when embedded into the hypercrystal, are slightly shifted in the physical space direction, away from the inner space located at B. Therefore, we also looked for a sign of a pure Al in our reconstructed densities inside the high symmetry two dimensional hyperplanes we discussed earlier, but now placed at the location of the embedded Al of $R(Al_{0.564}Cu_{0.116}Li_{0.320})$. These densities are shown in Fig. 14, where we could not detect any significant concentrations of the positive density that could be associated with Al at these locations.

A possibility that the Al is shifted in a physical space direction, away from the inner space at B, needs to be further investigated. Using Eqs. (4) and (5), we projected at each point of the inner space the density found in the physical space within a sphere of radius 0.5 Å surrounding that point. The result is shown in Fig. 15 where, indeed, we can see regions of high electron density along the 30 twofold axes around the Li hyperatom. Based on this observation, our initial analysis reported in Ref. 15 suggested a possibility of Al hyperatoms surrounding the Li hyperatom near B. However, we have now verified that these regions of high electron density originate, in fact, from densities at those E that are separated from the B by only 0.6 Å along the physical space so that their smeared densities are partially encompassed by the sphere of radius 0.5 Å.

III. CONCLUSION

Using the reconstructed x-ray and neutron structure factors of $i(Al_{0.570}Cu_{0.108}Li_{0.322})$, we determined and visualized density of scatterers in this quasicrystal. Our analysis of the densities in the associated six-dimensional hypercrystal finds that the densities are mainly peaked along three-dimensional sheets parallel to the inner space. The largest concentrations of the positive nuclear and electron densities occur around vertices. The electron density is depleted ex-

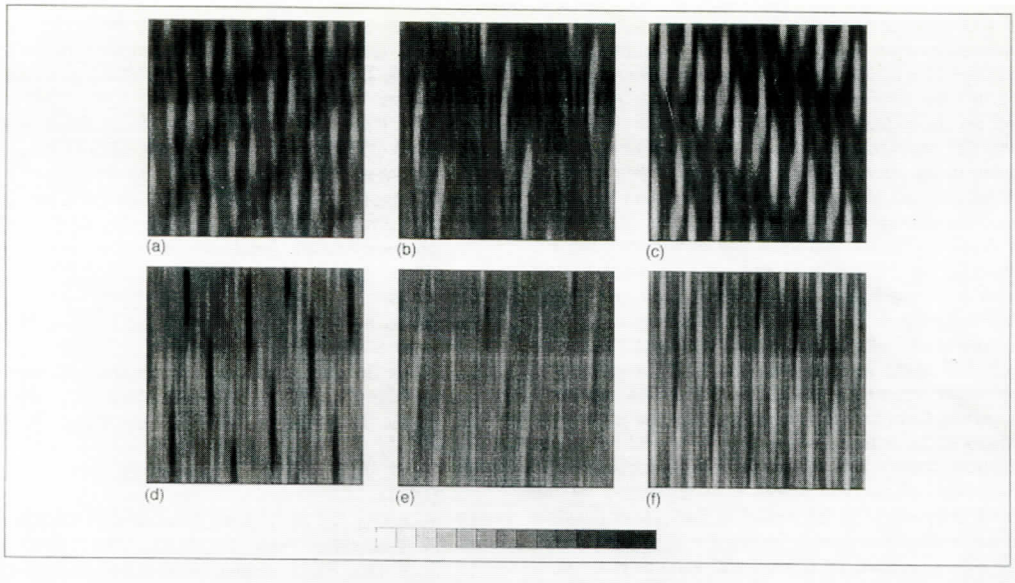

Figure 14. Reconstructed electron (first row) and nuclear (second row) densities in twofold (first column), threefold (second column), and fivefold (third column) symmetry planes at the embbing location of a pure Al atom of $R(Al_{0.564}Cu_{0.116}Li_{0.320})$. See Fig. 5 for the specific orientation of these planes and for the values of the gray scale map.

actly at vertices and it is somewhat extended along the fivefold symmetry axes. A slightly smaller peaks of positive nuclear and electron densities are also found around edge centers in a region that is oblate with respect to the fivefold axis (an edge projection) and somewhat extended along the twofold axes perpendicular to this axis. We found virtually no electron density, but a large negative nuclear density concentrated in regions around body centers, partially extended along the threefold axes. These observations are consistent with the stoichiometries and shapes of vertex, edge-center, and body-center hyperatoms determined in structural models of Refs. 15 and 16. Specifically, we conclude that the *B* hyperatom consists of Li and that its shape is qualitatively similar to a pentagonal dodecahedron with concave facets (i.e., it is extended along threefold axes and contracted along the fivefold axes). The *V* and *E* hyperatoms are a mixture of Al and Cu with a higher concentration of Cu at *V*. Shape of the *V* hyperatom is similar to a slightly rounded icosahedron (slightly wider along fivefold than threefold axes), with a small hole at its center. The *E* hyperatom should have an oblate shape with respect to its fivefold axis, with the equatorial cross section that is de-

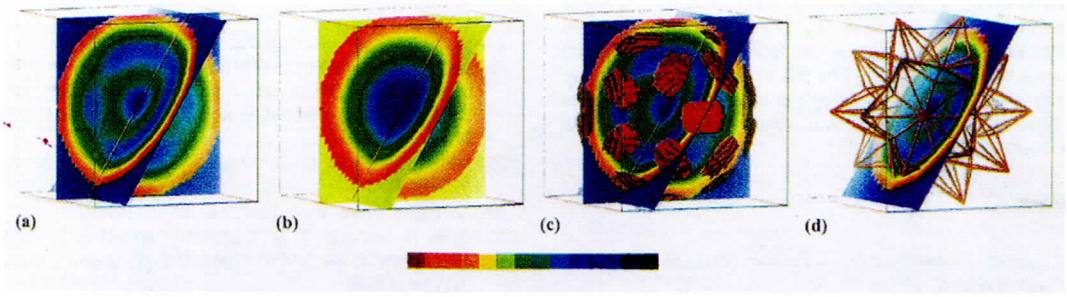

Figure 15. Reconstructed inner space density averaged over a physical space sphere of radius 0.5 Å. Same conventions as in Fig. 6 are used. The backgrounds for the electron and nuclear densities are set to 1.331 $eÅ^{-3}$ and 0.248×10^{-5} $Å^{-2}$, respectively. The dark blue color shown in the color map at the bottom of the figure, corresponds to the minimum values (0.311 $eÅ^{-3}$ and -7.496×10^{-5} $Å^{-2}$, for the electron and the nuclear density, respectively), while the red color corresponds to the maximum values (8.478 $eÅ^{-3}$ and 3.067×10^{-5} $Å^{-2}$, for the electron and the nuclear density, respectively). The isosurface in part (c) corresponds to the electron density of 7.735 $eÅ^{-3}$.

cagonal with vertices along the twofold axes. Although the above conclusions about the hyperatom shapes are qualitatively consistent with the structure models of Refs. 15 and 16, we could not find evidence of pure Al hyperatoms that surround the Li hyperatom in the model of Ref. 16. By analyzing the reconstructed density in terms of the Ammann tiling in the physical space, we found strong peaks of positive nuclear and electron densities at vertices and edge centers of the average tiles, and strong peaks of negative nuclear density near the two sites that divide the long PR diagonal in the ratio $\tau:1:\tau$, in accordance with several tiling models of i($Al_{0.570}Cu_{0.108}Li_{0.322}$). Furthermore, we found that the density inside the average RD was consistent with the structure model of Ref. 16 in that the electron density was decreased at the internal vertex and edge center sites, while a larger negative nuclear density peaks appeared slightly shifted from the internal edges, near the points that divide them in the ratio $\tau:1$. However, we could not find a high electron density, nor a high positive nuclear density, near the center of the RD where it is suggested by the location of the pure Al in the model of Ref. 16. A possible explanation of this discrepancy is that the symmetric decoration of RD, suggested in Ref. 55 and used in Ref. 16, is only appropriate for these RDs which are in local environments that are consistent with the symmetry of the decoration. Then, different decorations of RD will be appropriate in less symmetric environments, requiring shifts and substitutions of the atoms, in accord with our observations of split density peaks in the interior of the RD as well as along some of its external edges. However, in order to more accurately determine decorations of PRs, ORs, and RDs in different surroundings, it is first necessary to obtain more extensive experimental data and then extend the present work to more specific tiling arrangements.

Development of a computer package for modeling and visualizing reconstructed quasicrystal densities using the methods presented in this article is in progress. Until that work is completed, individual readers who intend to use our method or the programs as they become ready, should seek assistance from marko@sharac.tamu.edu.

ACKNOWLEDGMENTS

We are grateful to colleagues at the University of California Santa Cruz, particularly to G. Vallis and T. Schalk, for hospitality, assistance and the use of facilities while a part of this work was carried out. The 3D visualization figures in this paper were generated using the Application Visualization System. This research was supported in part by the NSF Grant No. DMR9215231.

REFERENCES

1. C. Janot, *Quasicrystals: A Primer* (Oxford University Press, Oxford, 1992).
2. *Quasicrystals: The State of the Art*, edited by D. P. DiVincenzo and P. J. Steinhardt (World Scientific, Singapore, 1991).
3. J. W. Cahn, D. Gratias, and B. Mozer, Phys. Rev. B **38**, 1638 (1988).
4. M. de Boissieu, C. Janot, J.-M. Dubois, M. Audier, and B. Dubost, J. Phys. (Paris) **50**, 1689 (1989).
5. S. van Smaalen, Phys. Rev. B **39**, 5850 (1989).
6. S.-Y. Qiu and M. V. Jarić, in *Quasicrystals*, edited by M. V. Jarić and S. Lundqvist (World Scientific, Singapore, 1989), p. 19.
7. J. W. Cahn, D. Gratias, and B. Mozer, Phys. Rev. B **38**, 1643 (1988); J. Phys. (Paris) **49**, 1225 (1988).
8. W. Steurer, Acta Cryst. B **45**, 534 (1989).
9. C. Janot, J. M. Dubois, and M. de Boissieu, in *Common Problems of Quasicrystals, Liquid Crystals, and Incommensurate Insulators*, edited by J. C. Tolédano (Plenum, New York, 1989), p. 9.
10. W. Steurer, Z. Cryst. **190**, 179 (1990).
11. S. van Smaalen, J. L. de Boer, and Y. Shen, Phys. Rev. B **43**, 929 (1991).
12. M. de Boissieu, C. Janot, J. M. DuBois, M. Audier, and B. Dubost, J. Phys.: Condens. Matter **3**, 1 (1991).
13. M. V. Jarić and S.-Y. Qiu, Acta Cryst. A **49**, 576 (1993).
14. M. V. Jarić and S.-Y. Qiu, Phys. Rev. B **49**, 6614 (1994).
15. S.-Y. Qiu and M. V. Jarić, Phys. Rev. B **52**, 894 (1995).
16. A. Yamamoto, Phys. Rev. B **45**, 5217 (1992).
17. S.-Y. Qiu, Ph.D. thesis, Texas A&M University, College Station, 1992 (unpublished).
18. C. R. Rowell, Senior thesis, University of California, Santa Cruz, 1994 (unpublished).
19. A. A. Besicovitch, *Almost Periodic Functions* (Cambridge University Press, Cambridge, 1932).
20. H. A. Bohr, *Almost Periodic Functions* (Chelsea, New York, 1947).
21. P. M. De Wolf, Acta. Cryst. A **28**, S111 (1972); **30**, 777 (1972).
22. A. Janner and T. Janssen, Phys. Rev. B **15**, 643 (1977); Physica **99**, 47 (1979); T. Janssen and A. Janner, Adv. Phys. **37**, 519 (1987).
23. D. Levine and P. J. Steinhardt, Phys. Rev. Lett. **53**, 2477 (1984).
24. P. A. Kalugin, A. Yu. Kitayev, and L. S. Levitov, Pis'ma Zh. Eksp. Teor. Fiz. **41**, 119 (1985) [JETP Lett. **41**, 145 (1985)].
25. P. Bak, Phys. Rev. Lett. **54**, 1517 (1985); Scr. Metall. **20**, 1199 (1986).
26. M. Duneau and A. Katz, Phys. Rev. Lett. **54**, 2688 (1985).
27. V. Elser, Phys. Rev. B **32**, 4892 (1985).
28. M. V. Jarić, J. Phys. (Paris) **C3-47**, 82 (1986); M. V. Jarić, in *Group Theoretical Methods in Physics*, edited by R. Gilmore (World Scientific, Singapore, 1987), p. 288.
29. M. V. Jarić and D. R. Nelson, Phys. Rev. B **37**, 4458 (1988).
30. V. Elser, Phys. Rev. Lett. **54**, 1730 (1985).
31. J. E. S. Socolar, T. C. Lubensky, and P. J. Steinhardt, Phys. Rev. B **34**, 3345 (1986); J. E. S. Socolar, *ibid.* **39**, 10519 (1989).
32. N. G. De Bruijn, Proc. Konig. Ned. Akad. Weten. A **84**, 39 (1981).
33. If an atomic tiling model is being tested, then the scale of the tiling cannot change by more than a couple of percents, certainly not by a factor of τ^3. This automatically fixes a particular order of inflation that should be used. Alternatively, if only certain tiling types without

a particular atomic decoration are considered, then the most appropriate order of inflation can be selected by the condition that it should result in the smallest number of distinct atomic decorations of the tiles.
34. P. Kramer, Acta Cryst. A **38**, 257 (1983).
35. M. Gardner, Sci. Am. **236**, 110 (1977).
36. A. L. Mackay, Physica A **114**, 66 (1983).
37. C. L. Henley, Phys. Rev. B **34**, 797 (1986).
38. M. Baake, S. I. Ben-Abraham, P. Kramer, and M. Schlottmann, in *Quasicrystals and Incommensurate Structures in Condensed Matter*, edited by M. J. Yacamán, D. Romeu, V. Castaño, and A. Gómez (World Scientific, Singapore, 1990), p. 85.
39. M. V. Jarić, Phys. Rev. B **34**, 4685 (1986).
40. A. Katz, Comm. Math. Phys. **118**, 263 (1988); A Katz, in *Introduction to the Mathematics of Quasicrystals*, edited by M. V. Jarić (Academic, New York, 1989), p. 147.
41. S. Narasimhan and M. V. Jarić, Phys. Rev. Lett. **62**, 454 (1989); M. V. Jarić and S. Narasimhan, Phase Transitions **16/17**, 351 (1989).
42. M. Duneau and C. Oguey, J. Phys. (Paris) **50**, 135 (1989).
43. K. N. Ishihara and P. H. Shingu, J. Phys. Soc. Jpn. **55**, 1795 (1986).
44. J. Komrska, Optik **80**, 171 (1987).
45. A larger x-ray diffraction data set is available [H. B. Elswijk, J. T. M. de Hosson, S. van Smaalen, and J. L. de Boer, Phys. Rev. B **38**, 1681 (1991)], but it has been obtained for a sample with unspecified density and stoichiometry. Therefore, we do not consider it in detail here. A comparison between this data set and the data set of Ref. 12 is more fully discussed in Ref. 46.
46. S.-Y. Qiu and M. V. Jarić, J. Non-Cryst. Solids **153&154**, 221 (1993).
47. Y. Ma, E. A. Stern, X.-O. Li, and C. Janot, Phys. Rev. B **40**, 8053 (1989).
48. M. de Boissieu, C. Janot, and J. M. Dubois, J. Phys.: Condens. Matter **2**, 2499 (1990).
49. X.-O. Li, E. A. Stern, and Y. Ma, Phys. Rev. B **43**, 1371 (1991).
50. K. Hiraga, in *Quasicrystals*, edited by T. Fujiwara and T. Ogawa (Springer, Berlin, 1990), p. 68.
51. H.-U. Nissen and C. Beeli, J. Non-Cryst. Solids **153&154**, 68 (1993).
52. H.-U. Nissen and C. Beeli, Int. J. of Mod. Phys. B **7**, 1387 (1993).
53. M. Audier, J. Pannetier, M. Leblanc, C. Janot, S. M. Dubost, and B. Dubost, Physica B **153**, 136 (1988).
54. See the review in Ref. 15 and references quoted therein.
55. C. L. Henley and V. Elser, Philos. Mag. Lett. **53**, L59 (1986).
56. M. V. Jarić and S.-Y. Qiu, J. Non-Cryst. Solids **153&154**, 181 (1993).
57. M. de Boissieu, R. J. Papoular, and C. Janot, Europhys. Lett. **16**, 343 (1991).
58. O. Radulescu and M. Kleman, J. Non-Cryst. Solids **153&154**, 227 (1993).

VIZUELNO PREDSTAVLJANJE I ANALIZA KVAZIKRISTALNIH GUSTINA

Ši-je Ču, Korbet R., Marko Vukobrat Jarić

Diskutovane su različite tehnike za vizuelno predstavljanje i analizu gustina centara rasejanja u kvaziperiodičnim kvazikristalima, kako u fizičkom tako i u pridruženom hiperprostoru. Uveden je i prikazan metod za analizu kvazikristalnih gustina na osnovu pločanja, i ilustrovan na primeru Amanovog ikosaedarskog pločanja. Posebno je primenjen na podatke za X i neutronsko rasejanje na $i(Al_{0.570}Cu_{0.108}Li_{0.322})$. Šestodimenzionalna hiperprostorna gustina od $i(Al_{0.570}Cu_{0.108}Li_{0.322})$ pokazala se konzistentnom sa slikom po kojoj su hiperatomi locirani u čvorovima, centrima ivica i centrima tela hiperkubne rešetke. U osnovnim crtama sugerisan je oblik hiperatoma. Pokazano je da su gustine nekih tačaka visoke simetrije u fizičkom prostoru slične $R(Al_{0.564}Cu_{0.108}Li_{0.322})$ kristalu, dok gustine oko drugih tačaka sugerišu nove atomske skupine. Amanovo pločanje pokazalo se kao korisna mustra za strukturu $i(Al_{0.570}Cu_{0.108}Li_{0.322})$, sa rombičnim dodekaedrima kao važnim gradivnim elementima. Iako se više strukturnih modela $i(Al_{0.570}Cu_{0.108}Li_{0.322})$ slaže sa rezultatima ove analize gustine, pronadjene su i neke razlike. Ispostavilo se da simtrična dekoracija rombičnog dodekaedra, slična onoj u $R(Al_{0.564}Cu_{0.110}Li_{0.320})$, koja je osnova različitih strukturnih modela, nije konzistentna sa analizom gusine. Nije pronadjen čisti Al unutar rombičnih dodekaedara, niti odgovarajući Al hiperatom u centru tela hiperkristala.